The Thesis committee for Taylor D. Niehues

certifies that this is the approved version of the following thesis:

Effects of Passive Parallel Compliance in Tendon-Driven Robotic Hands

APPROVED BY

SUPERVISING COMMITTEE:

Supervisor: _____
Ashish D. Deshpande

_____
Luis Sentis

Effects of Passive Parallel Compliance in Tendon-Driven Robotic Hands

by

Taylor D. Niehues, B.S.E.

THESIS

Presented to the Faculty of the Graduate School of

The University of Texas at Austin

in Partial Fulfillment

of the Requirements

for the Degree of

Master of Science in Engineering

THE UNIVERSITY OF TEXAS AT AUSTIN

December 2013

Acknowledgments

First, I would like to thank my advisor, Ashish Deshpande. Without his guidance and support, this research would not be possible.

I would also like to thank all the graduate and undergraduate students in the ReNeu Robotics Lab for the help they have given me, both in my research and in the writing of this thesis. Special thanks to Prashant Rao for his contributions in the tedious experimental setup and control of our testbed, and Pei-Hsin Kuo for his work in its design and construction.

Finally, I would like to thank the National Science Foundation for partially funding this research (grant # 1157954).

Effects of Passive Parallel Compliance in Tendon-Driven Robotic Hands

by

Taylor D. Niehues, M.S.E.
The University of Texas at Austin, 2013

SUPERVISOR: Ashish D. Deshpande

Humans utilize the inherent biomechanical compliance present in their fingers for increased stability and dexterity during manipulation tasks. While series elastic actuation has been explored, little research has been performed on the role of joint compliance arranged in parallel with the actuators. The goal of this thesis is to demonstrate, through simulation studies and experimental analyses, the advantages gained by employing human-like passive compliance in finger joints when grasping. We first model two planar systems: a single 2-DOF (degree of freedom) finger and a pair of 2-DOF fingers grasping an object. In each case, combinations of passive joint compliance and active stiffness control are implemented, and the impulse disturbance responses are compared. The control is carried out at a limited sampling frequency, and an energy analysis is performed to investigate stability. Our approach reveals that limited controller frequency leads to increased actuator energy input and hence a less stable system, and human-like passive parallel compliance can improve stability and robustness during grasping tasks. Then,

an experimental setup is designed consisting of dual 2-DOF tendon-driven fingers. An impedance control law for two-fingered object manipulation is developed, using a novel friction compensation technique for improved actuator force control. This is used to experimentally quantify the advantages of parallel compliance during dexterous manipulation tasks, demonstrating smoother trajectory tracking and improved stability and robustness to impacts.

Table of Contents

List of Tables

List of Figures

Chapter 1

Introduction

Robotic hands thus far have been unable to match the robust performance and graceful movements exhibited by human hands. Compliance and its modulation play an important role in the versatile performance of the human hands, which is achieved in spite of a significant inherent time delay ($>$100 ms [12]) in human reactions. Experiments show that humans have the ability to vary the stiffness in their joints, an ability that is used during both common and complex motions. For example, we stiffen our fingers and arms just before a perceived impact, in a preparatory response, by co-contracting antagonistic muscles to achieve robust grasping [11]. Also, biomechanical [13] and bio-mimetic [20] studies suggest that joint impedance modulation plays a key role in grasping stability. Our goal is to explore the role of compliance in the human hand, and implement compliance in robotic hands for improved performance.

Compliance in robots can be realized either actively or passively. Active stiffness control, or more generally, impedance control [10], uses sensor data and motor control to maintain a desired end-effector impedance. Many active control strategies have been implemented on existing robotic hands, e.g. joint stiffness control in the Robonaut 2 hand [1]. Object-level control has been implemented as well,

allowing the management of internal grasping forces [21] and leading to a variety of object grasping and manipulation strategies, such as for two-fingered grasping [3] or multi-finger object impedance control [18, 22]. These multi-contact control strategies have also been applied to compliant whole-body control of humanoid robots where multiple environmental contact points often occur [19]. An advantage of active stiffness or impedance control is that any desired impedance can be maintained explicitly in all directions. However, effective control using these methods requires that the actuator acts as a high-precision force source. Non-linearities and losses introduced through actuator gearing and transmission, such as friction, stiction and backlash, can deteriorate performance and make stable impedance control difficult. Also, because software has a finite reaction time, there is a threat posed by rigid impacts, which can damage actuators and reduce the robot's robustness [2]. Passive compliance, on the other hand, is implemented with mechanical spring elements. Passive mechanical compliance can be arranged in two distinct ways: in series with the actuators (e.g. through flexible tendons) and parallel to the actuators (e.g. through joint compliance). These two arrangements result in fundamentally different behavior and present unique control problems.

It has been shown that introducing passive mechanical compliance in series with the actuators can offer advantages such as backdriveability, better collision safety [16] and improved force control [17]. In robotic hands, series elastic elements are often introduced in the form of compliant tendons, such as in the DLR hand-arm system [9] and the five-fingered hand in the work by Yamano and Maeno [23]. The development of variable stiffness actuators [2] has built upon this idea

to allow explicit control of the mechanical stiffness of the end-effector, and controllers have been developed to simultaneously control the output joint torques and mechanical stiffness [6].

However, there are inherent stability issues and limitations that arise with series compliance. A desirable result of tendon-driven fingers is a low end-effector inertia. However, with springs in series with the tendons, the fingers may become unstable by violating the stability criterion of series elastic actuation [17]. This criterion specifies a minimum load inertia, as a light load inertia may resonate with the series elasticity. Also, for precise impedance control, series elastic tendon-actuated systems depend upon accurate tension sensing through either force sensors or spring displacement feedback. Noise and inaccuracies in sensors will limit the system's performance. Looking at a grasping situation for a robotic hand with series compliance, the work by Cutkosky and Kao [7] presents stability thresholds for compliant fingers performing two-fingered grasps. For tasks involving smaller objects or fingers with more compliant elastic elements, generating the required grip forces may result in a highly unstable system which cannot be effectively stabilized by active control.

Passive compliance can also be arranged in parallel to the actuators. In human hands, the ligaments and joint capsules lead to compliance at the joint which is in parallel to muscle and tendon compliance. This parallel compliance plays an important role in achieving robust and smooth grasping and manipulation. When performing dexterous manipulation tasks with robotic hands, precise force and position control along with highly stable and impact-resistant fingers are critical. The

addition of parallel passive compliance, inspired by the human compliance, may prove beneficial in this regard. However, limited research has been carried out to analyze the effects of parallel compliance when implemented in robotic hands. There are a few example of robots with parallel passive compliance. In the SDM Hand [8], parallel compliance is used in under-actuated fingers to enable successful grasping with uncertainty in target object location. The UB Hand 3 [14] is designed with inherent joint compliance in parallel with the actuators to improve grasp stability and adaptability. However, current works either do not extend to fully actuated hands or do not analyze the effects of parallel compliance.

The goal of this paper is to demonstrate, through mathematical modeling and simulation analysis, the advantages gained by employing passive compliance in finger joints. From a controls perspective, the aforementioned neuromuscular time delay should severely limit human performance, yet we still display robust manipulation capabilities. Passive compliance may be playing a key role in this regard. We want to determine if passive compliance can be proven to be similarly beneficial for robotic systems, or if this compliance is simply how the human body has evolved overcome its relatively slow response time. This study may lead to a better understanding of human biomechanics and controls.

We begin with a simulation study to identify the benefits of passive compliance in the presence of a limited controller sampling rate. Controller speed limitations are inevitable in robotic systems, especially in systems with large numbers of actuators and sensors such as robotic hands. A single 2-DOF finger is modeled and its disturbance response is analyzed, first with passive human-like joint stiff

and then with an active joint stiffness controller with a limited controller frequency. A passivity analysis is performed for each case to determine the energy flow in the system and its effects on stability.

Then, inspired by the passive properties present in the human hand, we hypothesize that introducing compliance in parallel with the actuators in robotic hands will improve stability, robustness, and trajectory smoothness during object grasping and manipulation. For this, we present a more involved scenario with two fingers grasping an object. The contacts are modeled as point contacts, and the motion of the system is assumed to be constrained to a horizontal plane. The system implements an object-level stiffness control law, and again the controller sampling rate is limited. Then, passive joint stiffness is introduced to the joints in parallel with the actuators. Grasp performance and stability is analyzed for each case, similar to the qualitative measures presented in [4].

We then develop a more complex impedance controller for an experimental testbed, first for joint impedance control of a single 2-DOF finger and then for object grasping and manipulation using two 2-DOF tendon-driven fingers. Then we experimentally quantify the advantages of parallel joint compliance in grasping scenarios. Using an object impedance control strategy to allow environment interaction, we compare a case without passive compliance and another case with joint compliance parallel to the actuators in the form of flexible ligaments. We use trajectory tracking accuracy and robustness to impacts as performance metrics.

Chapter 2

Modeling of Tendon-Driven Robotic Finger System

We begin by deriving the dynamic model of a planar 2-DOF robotic finger with a 2N tendon arrangement, as in Fig. 2.1. Notice that a nonlinear joint stiffness term $\boldsymbol{\tau}_k(\mathbf{q})$ is included for generality. Then, we extend this model to two robotic fingers grasping an object, as in Fig. 2.2.

Variable	Description
$\mathbf{q} \in \mathbb{R}^2$	joint positions
$\boldsymbol{\theta} \in \mathbb{R}^4$	motor positions
$\mathbf{M} \in \mathbb{R}^{2\times 2}$	link side inertia matrix
$\mathbf{C} \in \mathbb{R}^2$	link side centrifugal, Coriolis, and damping terms
$\boldsymbol{\tau}_k \in \mathbb{R}^2$	nonlinear joint stiffness term
$\mathbf{f}_t \in \mathbb{R}^4$	tendon forces
r_1, r_2	radii of joint pulleys
$\mathbf{l}(\mathbf{q}) \in \mathbb{R}^4$	tendon inverse kinematics (joint-to-tendon space)
$\mathbf{R} \in \mathbb{R}^{2\times 4}$	tendon mapping matrix
$\mathbf{R}^+ \in \mathbb{R}^{4\times 2}$	generalized pseudo-inverse of $\mathbf{R}$
$\mathbf{f}_{int} \in \mathbb{R}^4$	internal tendon forces, acting in null-space of $\mathbf{R}$
$\mathbf{J}(\mathbf{q}) \in \mathbb{R}^{2\times 2}$	Jacobian matrix (joint to Cartesian coordinates)
$\mathbf{f}_{ext} \in \mathbb{R}^2$	Cartesian forces exerted at fingertips
$\mathbf{J}_m \in \mathbb{R}^{4\times 4}$	diagonal matrix of motor inertias
$\boldsymbol{\tau}_{\theta,fr} \in \mathbb{R}^4$	motor frictional torques
$\mathbf{P}_m \in \mathbb{R}^{4\times 4}$	diagonal matrix of motor pulley radii
$\boldsymbol{\tau}_{\theta,m} \in \mathbb{R}^4$	input motor torques

Table 2.1: Description of variables used for 2-DOF tendon-driven finger.

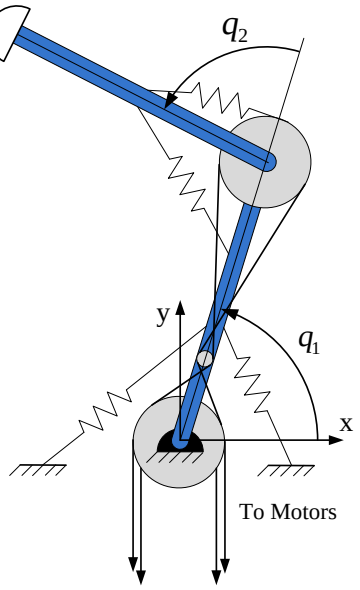

Figure 2.1: 2-DOF tendon-driven robotic finger. Two tendons are connected to the first joint q_1, and the other two wrap around an idler pulley at joint 1 and attach to the second joint q_2. Parallel joint compliance is represented by ligament-like springs that span the joints.

2.1 2-DOF Antagonistic Tendon-Driven Finger

Using the variables defined in Table 2.1, the state equations for the tendon-driven 2-DOF finger shown in Fig. 2.1 can be represented as

$$\mathbf{M}(\mathbf{q})\ddot{\mathbf{q}} + \mathbf{C}(\mathbf{q},\dot{\mathbf{q}}) + \boldsymbol{\tau}_k(\mathbf{q}) = \mathbf{R}\mathbf{f}_t + \mathbf{J}(\mathbf{q})^T\mathbf{f}_{ext} \tag{2.1}$$

$$\mathbf{J}_m\ddot{\boldsymbol{\theta}} + \boldsymbol{\tau}_{\theta,fr} + \mathbf{P}_m\mathbf{f}_t = \boldsymbol{\tau}_{\theta,m} \tag{2.2}$$

Knowing the tendon inverse kinematics $\mathbf{l}(\mathbf{q})$ relating joint positions to ten-

don positions, the tendon map matrix is found through differentiation.

$$\mathbf{R} = \left(\frac{\partial \mathbf{l}(\mathbf{q})}{\partial \mathbf{q}}\right)^T = \begin{bmatrix} r_1 & -r_1 & r_1 & -r_1 \\ 0 & 0 & r_2 & -r_2 \end{bmatrix} \tag{2.3}$$

Then, the principle of virtual work yields the two relations

$$\dot{\mathbf{l}} = \mathbf{R}^T \dot{\mathbf{q}}, \qquad \boldsymbol{\tau}_q = \mathbf{R}\mathbf{f}_t \tag{2.4}$$

This tendon mapping matrix $\mathbf{R}$ will be used extensively by the control algorithms.

2.2 Two-Fingered Object Manipulation

An important goal for robotic hands is the ability to robustly grasp and manipulate objects. To fully understand the effects of finger compliance on robotic hand performance, we present the task of two-finger grasping. Because of the natural instability of two-fingered pinching, active control must be used to robustly stabilize the grasp while also performing some desired object motions or environment interactions.

We start with a model of the entire system, shown in Fig. 2.2. The dynamic equations of motion for each finger $i = 1, 2$ are identical to Eqs. (2.1) and (2.2). The external force vector $\mathbf{f}_{ext,i}$ in Eq. (2.1) for each finger i will also include the opposing reactions from the hard-finger contact forces being applied to the object, $\mathbf{f}_{c,i}$, which can be expressed in the global (x,y) frame as

$$\mathbf{f}_{ci} = \begin{bmatrix} \cos(\phi) & -\sin(\phi) \\ \sin(\phi) & \cos(\phi) \end{bmatrix} \begin{bmatrix} (-1)^{i+1} f_i \\ \lambda_i \end{bmatrix} \tag{2.5}$$

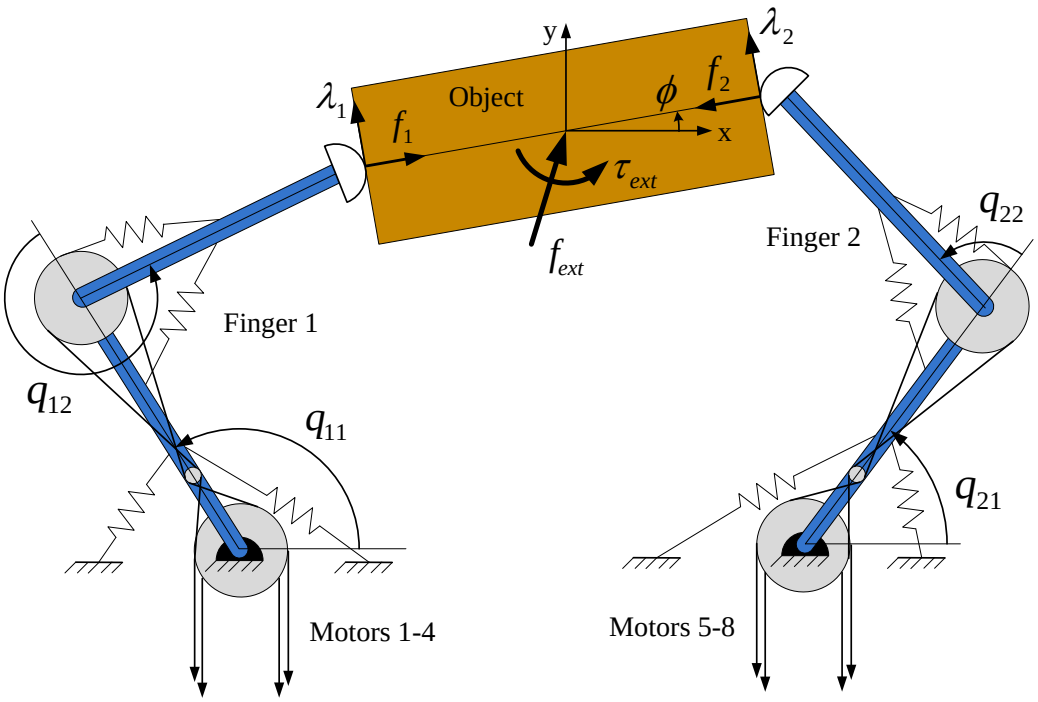

Figure 2.2: Model of two 2-DOF fingers grasping an object. Contact points are modeled as hard-finger contacts, meaning the fingers can exert both normal forces and tangential frictional forces on the object.

where f_i and λ_i are the normal and tangential forces, oriented as in Fig. 2.2. In the controller, these contact forces are modeled as point contacts between the fingertips and the object.

The object dynamics are modeled as

$$m_{obj}\begin{bmatrix}\ddot{x}\\ \ddot{y}\end{bmatrix} = \mathbf{f}_{c1} + \mathbf{f}_{c2} + \begin{bmatrix}f_{ext,x}\\ f_{ext,y}\end{bmatrix} \tag{2.6}$$

$$I_{obj}\ddot{\phi} = \frac{1}{2}w_{obj}(\lambda_2 - \lambda_1) + \tau_{ext} \tag{2.7}$$

where m_{obj}, I_{obj}, and w_{obj} are the object's mass, inertia about the z-axis, and width,

respectively. For this system, it is assumed that the object's C.O.M. is located midway between the contact points. The terms $f_{ext,x}$, $f_{ext,y}$, and τ_{ext} are the external forces and moment being exerted on the object.

Chapter 3

Simulation Studies

We perform simulations to analyze the disturbance responses for various cases. First, we simulate a single 2-DOF tendon-driven finger implementing an active stiffness controller, specifically analyzing the effect of a limited controller sampling rate on system stability. We then simulate a two-fingered pinching grasp utilizing an object-level stiffness controller. For this, we again look at the effect of controller sampling rate, but also analyze the effect of adding parallel joint compliance (e.g. elastic ligaments) to the fingers.

3.1 Single 2-DOF Tendon-Driven Finger: Human-Like Stiffness

We would like to reproduce a human-like nonlinear stiffness profile in the robotic fingers. For simulation purposes, we assume that the tendon actuators act as ideal force sources, such that they are able to produce any combination of desired joint torques ($\boldsymbol{\tau}_q = \mathbf{R}\mathbf{f}_t = \boldsymbol{\tau}_{q,des}$). There is no passive mechanical stiffness present ($\boldsymbol{\tau}_k = 0$).

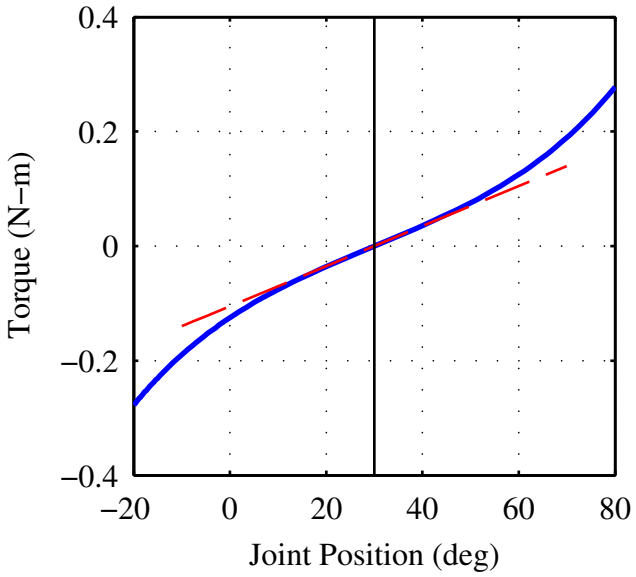

Figure 3.1: A human-like nonlinear torque profile, shown for a joint with the stiffness profile in Eq. (3.1) with $\alpha = 0.05\ \frac{N \cdot m}{rad}$ and $\beta = 2$, resulting in a linearized stiffness of $k_q = 0.2\ \frac{N \cdot m}{rad}$ (red dotted line) at the equilibrium position $q = \pi/6 = 30^o$.

3.1.1 Joint Stiffness Controller Design

We model the active stiffness controller torque $\boldsymbol{\tau}_{q,des}$ to mimic the index finger MCP joint stiffness profile, simplified from the double exponential joint stiffness equation presented in [13] as:

$$\tau_{q,des_i}(q_i) = -\alpha(e^{-\beta \Delta q_i} - e^{\beta \Delta q_i}) \tag{3.1}$$

for fingers $i = 1, 2$, where $\Delta q_i = q_i - q_{i,0}$, and $q_{i,0}$ is the joint equilibrium position.

The value of the constant β is chosen to be equal to that from the model derived for one subject in [13] to produce a human-like stiffness curve. The other constant α is scaled such that the linearized stiffness around the equilibrium point

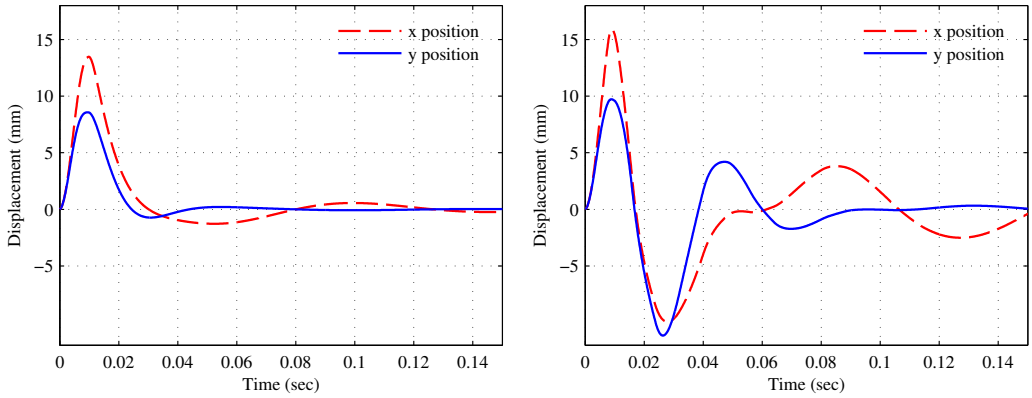

(a) (b)

Figure 3.2: The x-y impulse response of a human-like active stiffness controller, with (a) infinite controller frequency, and (b) an 8 ms sampling rate (125 Hz controller frequency).

of each joint can be set to some desired value k_q for each joint:

$$\left.\frac{\partial \tau_{q_i}}{\partial \Delta q}\right|_{\Delta q=0} = 2\alpha\beta = k_q \tag{3.2}$$

An example of the nonlinear torque profile produced with k_q = 0.2 $\frac{N \cdot m}{rad}$ is shown in Fig. 3.1.

3.1.2 Simulation Results

In each simulation, the endpoint of the finger is subjected to a 10 N impulse lasting 0.01 seconds in the positive y-direction. Linear viscous joint damping is introduced in the form $d_q[\dot{q}_1, \dot{q}_2]^T$. The equilibrium positions were chosen to be $q_1 = \pi/6$ and $q_2 = \pi/2$, and finger lengths and masses of L_1 = L_2 = 0.03 m and M_1 = M_2 = 0.03 kg were used, with the link inertias modeled as simple rods.

At the equilibrium point, the desired linearized stiffness for each joint is

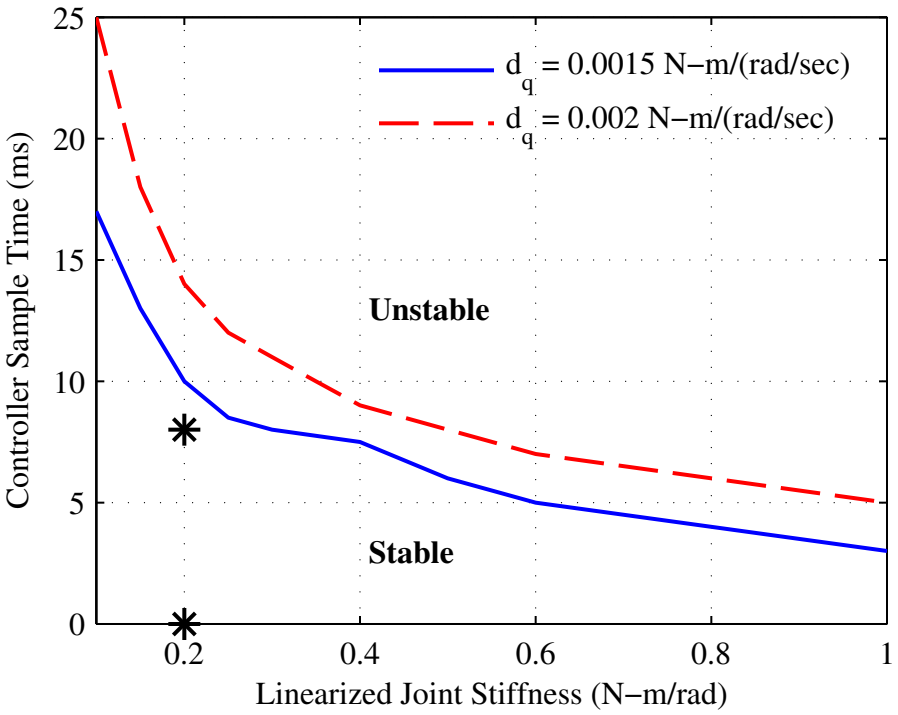

Figure 3.3: Observed stability boundary conditions for a single finger with variations in joint stiffness, viscous damping, and controller sampling times. The two cases shown in Fig. 3.2 (with $d_q = 0.0015 \frac{N \cdot m}{rad/sec}$) are marked with asterisks.

chosen, and the required constants for Eq. (3.1) were found accordingly using Eq. (3.2). An example of the generated torque profile is shown in Fig. 3.1. The limited controller frequency is implemented such that torques being produced by the actuators $\boldsymbol{\tau}_{q,des}$ are calculated discretely at a given time interval, using joint position data at that time instant as feedback.

Multiple impulse response simulations are performed, with varying values of joint stiffness, viscous damping, and controller frequency. Examples of two impulse response simulations are shown in Fig. 3.2. A summary of the relationship

between these three parameters is illustrated by the results shown in Fig. 3.3. Fingers with lower joint stiffness gains or with higher damping values are less likely to go unstable with lower sampling rates. However, in practice, implementing low stiffness gains and high joint damping in a finger would result in sluggish reactions and poor performance due to unmodeled friction and uncertainties.

This study shows the limitations of using active control to implement a desired joint stiffness in robotic fingers. To analyze the source of the observed instabilities in these simulations, we will observe the energy flow in the system.

3.1.3 Energy and Passivity Analysis

The first case with infinite controller frequency acts as the equivalent of a purely mechanical system, resulting in an inherently passive system. For the cases with limited sampling rates, on the other hand, we analyze the energy input and output of the system to observe the passivity properties. Taking the inner product between $\dot{q}$ and the finger equations of motion in Eq. (2.1) and replacing $\mathbf{R}\mathbf{f}_t$ with a generalized torque input $\mathbf{u}$ yields

$$\dot{\mathbf{q}}^T\mathbf{u} = \frac{d}{dt}(KE) + d_q\|\dot{\mathbf{q}}\|^2 - \dot{\mathbf{q}}^T(\mathbf{J}(\mathbf{q})^T\mathbf{f}_{ext}) \tag{3.3}$$

where KE is the kinetic energy of the finger, expressed as

$$KE = \frac{1}{2}\dot{\mathbf{q}}^T\mathbf{M}(\mathbf{q})\dot{\mathbf{q}} \tag{3.4}$$

Equation (3.3) represents the power relation of the system, where the left side contains the actuator energy input and the right side contains the kinetic energy,

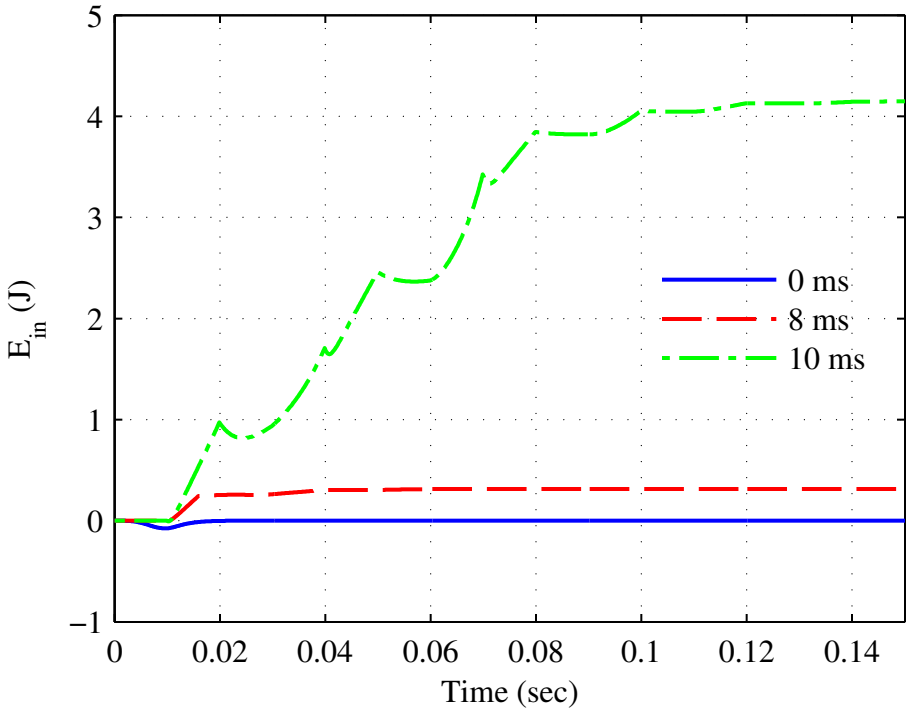

Figure 3.4: The actuator energy input (E_{in}) to the system with varying controller sampling rate.

dissipative losses, and external energy input. Rearranging and integrating this leads to the energy relation

$$\begin{aligned} KE(t) - KE(0) &= \int_0^t \left(\dot{\mathbf{q}}^T \mathbf{u} + \dot{\mathbf{q}}^T (\mathbf{J}(\mathbf{q})^T \mathbf{f}_{ext}) - d_q \|\dot{\mathbf{q}}\|^2 \right) d\tau \\ &= E_{in} + E_{ext} - E_{diss} \end{aligned} \tag{3.5}$$

The E energy terms defined here represent the cumulative energy input/output to the system, with E_{in} coming from the actuators, E_{ext} from the external forces, and E_{diss} from the passive viscous joint damping. As a general rule, stability comes as the result of a decrease in the kinetic energy of the system over time. Since we

cannot control the E_{ext} or E_{diss} terms through active control, our focus should be on minimizing actuator energy input $E_{in} = \int_0^t (\dot{\mathbf{q}}^T \mathbf{u}) d\tau$.

A plot of the actuator energy input to the system, given parameter values of $k_q = 0.2 \frac{N \cdot m}{rad}$ and $d_q = 0.0015 \frac{N \cdot m}{rad/sec}$ and with varying sampling rates, is shown in Fig. 3.4. In an ideal system with an infinite controller frequency, active stiffness control does not add energy to the system because it emulates a purely mechanical system, resulting in passivity. However, as controller limitations are introduced, we observe that the actuators add energy to the system. If this energy input becomes high enough to overcome the energy dissipation term, the system becomes unstable. Referring to Fig. 3.3, with these stiffness and damping parameters the 10 ms plot line in Fig. 3.4 represents the borderline stable case.

3.2 Two-Finger Object Pinching

Next a two-fingered pinch grasping scenario is presented. These simulations are designed to analyze the effects of both controller frequency and passive parallel joint compliance on the impulse response of the system. Once again, we assume the actuators are ideal force sources, such that the desired joint torques can be produced instantaneously. The passive parallel compliance is introduced in the form of a human-like nonlinear stiffness given by Eq. (3.1).

3.2.1 Object-Level Stiffness Control Design

For robust performance in the presence of unknown disturbances in the environment, we implement object-level stiffness control [18]. Letting $\mathbf{z} = [x, y, \phi]^T$

represent the object's position and orientation, we define the desired contact forces to be exerted on the object by the fingertips as a stiffness behavior:

$$\mathbf{f}_{cmd} = \mathbf{W}^{+}\mathbf{K}_{d}(\mathbf{z}_{des} - \mathbf{z}) \tag{3.6}$$

Here, $\mathbf{W}^{+}$ is the pseudoinverse of the grasp matrix, which is found from the relation

$$\begin{bmatrix} \mathbf{f}_{xy,obj} \\ \tau_{obj} \end{bmatrix} = \mathbf{W} \begin{bmatrix} \mathbf{f}_{c1} \\ \mathbf{f}_{c2} \end{bmatrix} \tag{3.7}$$

where $\mathbf{f}_{xy,obj}$, τ_{obj} contain the forces and moments applied to the object by the fingers, $\mathbf{f}_{ci}$ are the contact forces at each fingertip, and $\mathbf{W} \in \mathbb{R}^{3\times4}$ defines the grasp matrix. Matrix $\mathbf{K}_{d} = diag(k_x, k_y, k_\phi)$ contains the object stiffness gains. Then, the four desired joint torques are:

$$\boldsymbol{\tau}_{q,des} = \mathbf{J}^{T}\Big(\mathbf{f}_{cmd} + \begin{bmatrix} \mathbf{f}_{grip,1} \\ \mathbf{f}_{grip,2} \end{bmatrix}\Big) + \begin{bmatrix} \boldsymbol{\tau}_{k,1}(\mathbf{q_1}) \\ \boldsymbol{\tau}_{k,2}(\mathbf{q_2}) \end{bmatrix} \tag{3.8}$$

where $\mathbf{J} = diag(\mathbf{J}_1(\mathbf{q}_1), \mathbf{J}_2(\mathbf{q}_2))$ contains the Jacobian matrices for both fingers, and $\boldsymbol{\tau}_{k,i}$ is a feedforward term to compensate for any passive joint compliance we may choose to implement. $\mathbf{f}_{grip,i}$ (i = 1,2) are vectors in the null-space of $\mathbf{W}$ which are used to produce a desired grip force $f_{grip,des}$. For this system, the two force vectors $\mathbf{f}_{grip,i}$ are equal and opposite with a line of action passing through the two contact points. To enforce $f_{grip,des}$, we use Eq. (2.5):

$$\mathbf{f}_{ci} = \begin{bmatrix} \cos(\phi) & -\sin(\phi) \\ \sin(\phi) & \cos(\phi) \end{bmatrix} \begin{bmatrix} (-1)^{i+1} f_i \\ \lambda_i \end{bmatrix}$$

with $\lambda_i = 0$ and $f_i = f_{int}$, where f_{int} is defined as

$$f_{int} = f_{grip,des} - \min_{i=1,2}(-1)^{i+1}(f_{xi}cos(\phi) + f_{yi}sin(\phi)) \tag{3.9}$$

Note that this feedback control takes the object position and orientation as input, and has no knowledge of the external forces being applied.

3.2.2 Simulation Results

The dual finger parameters are set as L_1 = L_2 = 0.03 m and M_1 = M_2 = 0.03 kg, and the grasped object is modeled as a cuboid with width w = 0.1 m, height h = 0.05 m, mass M_{obj} = 0.05 kg, and inertia $I_{obj} = \frac{1}{12} M_{obj}(w^2 + h^2)$. An impulse was applied to the object as $f_{ext,x}$ = $f_{ext,y}$ = 3 N and τ_{ext} = 0.2 N·m, each lasting 0.03 seconds. Joint viscous damping is introduced as $0.0015 \frac{N \cdot m}{rad/sec} \cdot [\dot{q_1}, \dot{q_2}]^T$. The initial finger positions are set to $q_{11} = 2\pi/3$, $q_{12} = -\pi/2$, $q_{21} = \pi/3$, and $q_{22} = \pi/2$, and the initial object orientation is $\phi = 10^\circ$. The controller acts to maintain this position and orientation through the presented stiffness control law. The object stiffness gains were set to k_x = k_y = 500 N/m and $k_\phi = 2 \frac{N \cdot m}{rad}$, and the desired gripping force is set to $f_{grip,des}$ = 5 N.

We first ran simulations with no passive joint compliance present. Figure 3.5(a) shows the relatively stable impulse response of this system with no controller frequency limitations. The next simulation used a 200 Hz controller frequency, which caused a less stable, oscillatory response, as shown in Fig. 3.5(b).

To see the effects of passive parallel compliance, human-like elastic elements were introduced at each joint. The constants were chosen to be $\alpha = 0.25 \frac{N \cdot m}{rad}$ and $\beta = 2$, resulting in a linearized stiffness of k_q = 1 $\frac{N \cdot m}{rad}$ at the equilibrium positions of all the joints. Fig. 3.5(c) shows the results with the same 200 Hz controller and with parallel passive joint compliance. When compared to Fig. 3.5(b), we see

that the passive compliance has improved the stability of the system.

The internal gripping forces produced by the fingers, shown in Fig. 3.6(a), all tracked to the desired $f_{grip,des}$ = 5 N. Even with an infinite controller sampling rate, we do not expect this force to track perfectly, as our controller had no knowledge of external forces and also did not compensate for the fingers' inertia or damping. While all three simulation cases displayed similar grip forces, the addition of passive compliance causes the grip force to settle more quickly to the desired $f_{grip,des}$ due to its more stable motion.

Another related factor when analyzing grasp stability is the prevention of slippage at the contact points. Figure 3.6(b) shows the ratio of tangential and normal forces. If this value stays below the coefficient of friction at the contact points, then no slippage will occur. Again, the three cases displayed similar responses at impact, but we can see after the initial impact, the addition of joint compliance helps the system recover more quickly and keep this friction force ratio lower.

3.2.3 Analysis of Results and Discussion

To analyze the underlying reasons for this increased stability, we isolated the combined torques being produced by the actuator and compliant element at any single joint q at time t. From Eq. (3.8), the control torque is defined as $\tau_{q,des} = \tau_{q,cmd} + \tau_k(q)$, where $\tau_k(q)$ is the feed-forward torque to compensate for the joint stiffness, and $\tau_{q,cmd}$ is torque required to produce the designated object-level stiffness forces and grip forces. Then, the combined actuator and joint spring torque

is:

$$\tau_{total}(t) = \tau_{q,des} - \tau_k(q) = \tau_{cmd} \tag{3.10}$$

For an accurate model where $\tau_{k,est} = \tau_k$, the torques produced at each joint are simply the object-level torques $\tau_{q,cmd}$, as expected. In the ideal case, this system's response would behave identically with or without passive joint compliance, because the controller is designed to compensate for the joint stiffness.

However, as Δt time passes during a time delay interval and the joint angle changes by Δq, the control torque $\tau_{q,des}$ remains the same, but the combined actuator/spring torque becomes

$$\tau_{total}(t + \Delta t) = \tau_{q,des} - \tau_k(q + \Delta q) = \tau_{cmd} + \Delta\tau \tag{3.11}$$

where

$$\Delta\tau = \tau_k(q) - \tau_k(q + \Delta q) \tag{3.12}$$

With a positive joint stiffness and an accurate joint compliance model in the controller, $\Delta\tau$ in Eq. (3.12) will act in the opposite direction of Δq. Intuitively, this means the $\Delta\tau$ term produces a resistive effect in the system, opposing the direction of the joint's velocity. From an energy perspective, this resistive torque acts as an energy dissipator.

In the case of a nonlinear stiffness profile, this resistive effect will be more pronounced as the finger moves toward its joint limits, an ideal characteristic for manipulation tasks. In the working range close to the equilibrium position, less resistance produces faster responses. As the finger moves toward its joint limits,

the higher linearized joint stiffness produces a greater resistive effect, dissipating more energy and improving stability.

These conclusions offer further evidence that passive parallel compliance improves the robustness of human grasping, especially considering humans must overcome neuromuscular time delays that are an order of magnitude higher than what we have simulated here ($>$ 100 ms [12]). Therefore, integrating passive compliance in the design of robotic hands may prove to be beneficial and could narrow the performance gap between the robotic and human hands. In the next section, experiments with tendon-driven robotic fingers are performed verify and expand upon these simulation results.

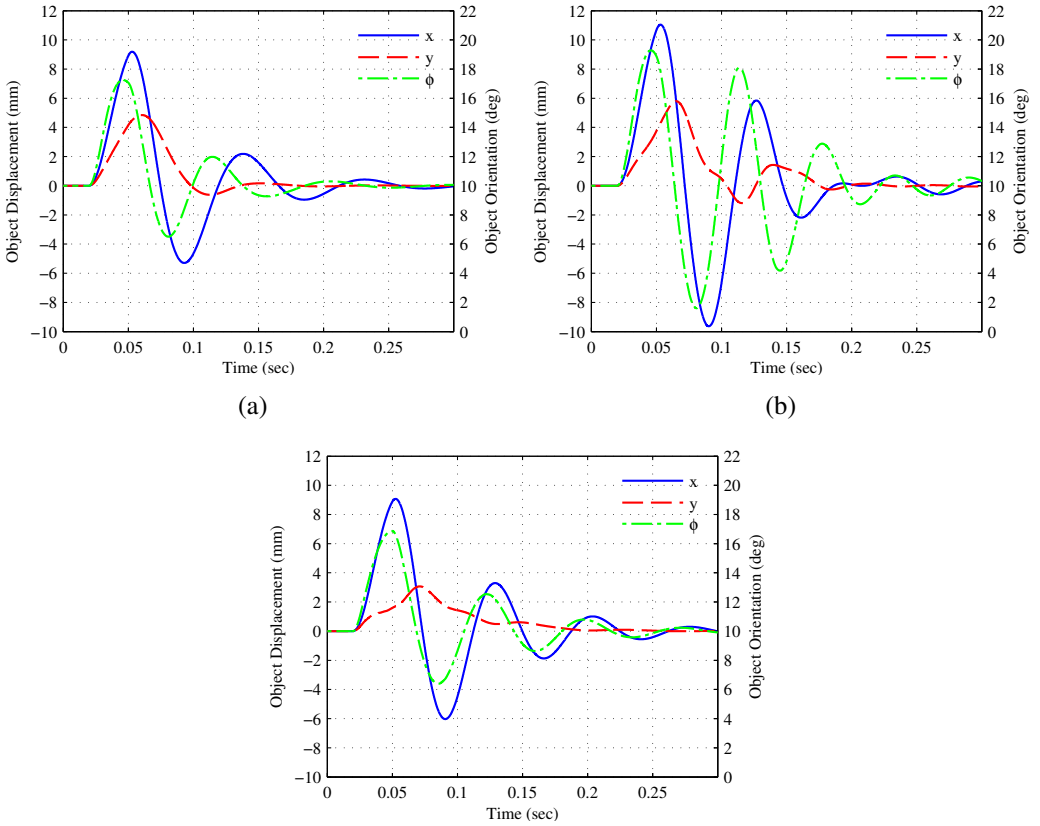

Figure 3.5: Simulations of two-fingered pinching grasps subjected to impacts. First are the position responses for the gripped object with (a) infinite controller sampling frequency, (b) a 200 Hz controller frequency and no passive joint compliance, and (c) a 200 Hz controller frequency with human-like parallel joint compliance present, linearized to $k_q = 1.0 \frac{N \cdot m}{rad}$ at equilibrium. We can see that the addition of parallel compliance works to counteract the destabilizing effects of a limited sampling rate.

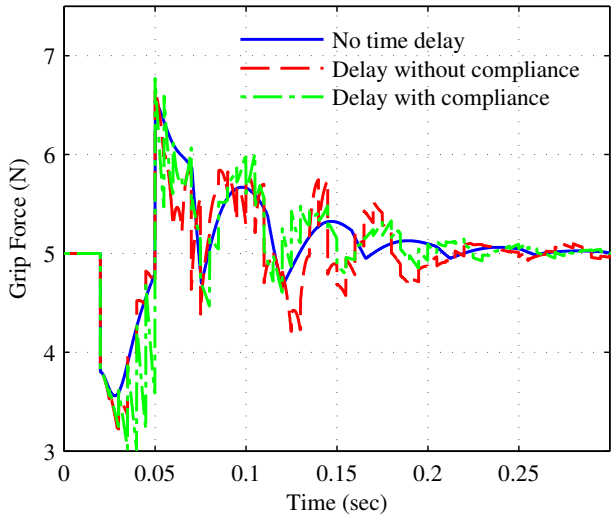

(a)

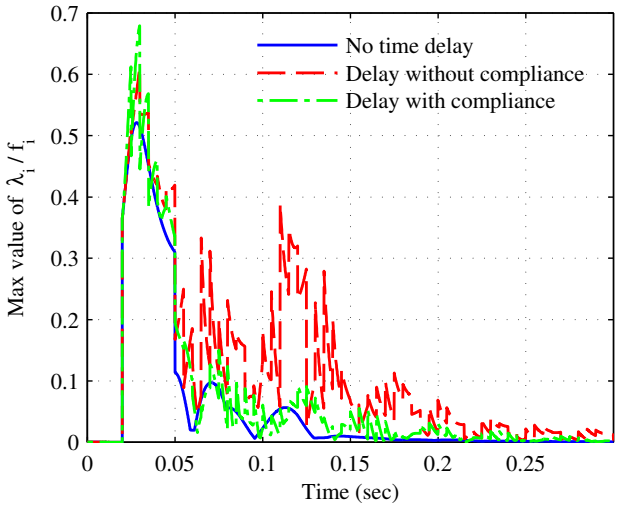

(b)

Figure 3.6: Contact forces for the two-fingered pinching simulations of Fig. 3.5. (a) The internal grip forces present for each case. (b) The slip condition at the point contacts, shown as the larger value of λ_i / f_i at the contact points of fingers $i = 1, 2$. If this value rises above the coefficient of friction at the contact point, slippage will occur. The addition of compliance does not lower slip condition at the time of impact, but does cause faster settling to a lower value due to its increased stability.

Chapter 4

Experimental Study: Effects of Parallel Compliance in Robotic Fingers

In this section, we present the results of experiments carried out to validate the findings of the simulation study in the previous section that parallel joint compliance improves stability of fingers, especially in grasping and manipulation tasks. We will give an overview of the hardware and software setup, expand the previous control law to improve performance in this testbed, and explain our findings.

4.1 Experimental Setup

Experimental implementation of tendon-driven fingers that are capable of performing dexterous manipulation tasks required a robust hardware and software platform. Since we want to focus on the effects of parallel compliance on the system, we needed to ensure that the end effector remained as light as possible, sensors and actuators were well integrated and control loops were deterministic. In this section we discuss the details of the various components of our experimental testbed.

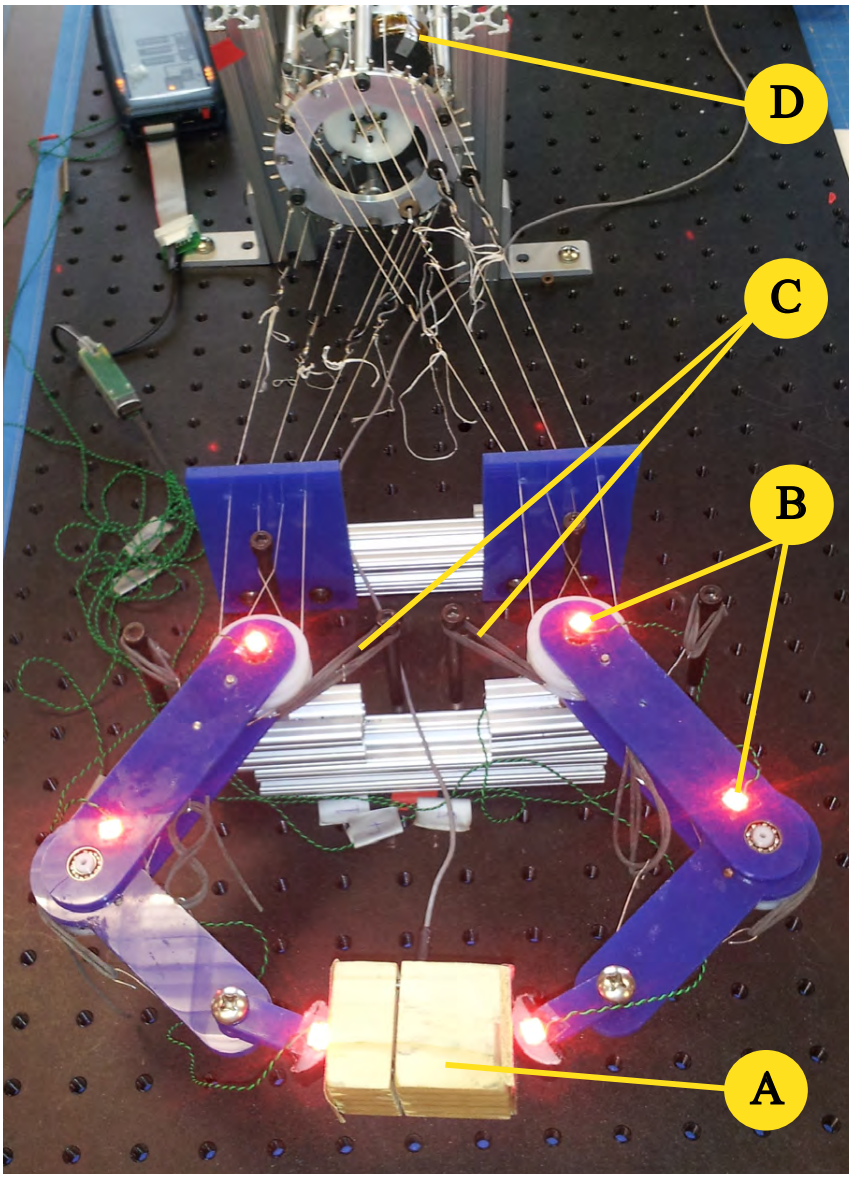

Figure 4.1: Hardware setup for the experiments. A) Button cell force sensor in wooden enclosure. B) Motion capture LED markers. C) Parallel joint compliance. D) Custom built BLDC motors.

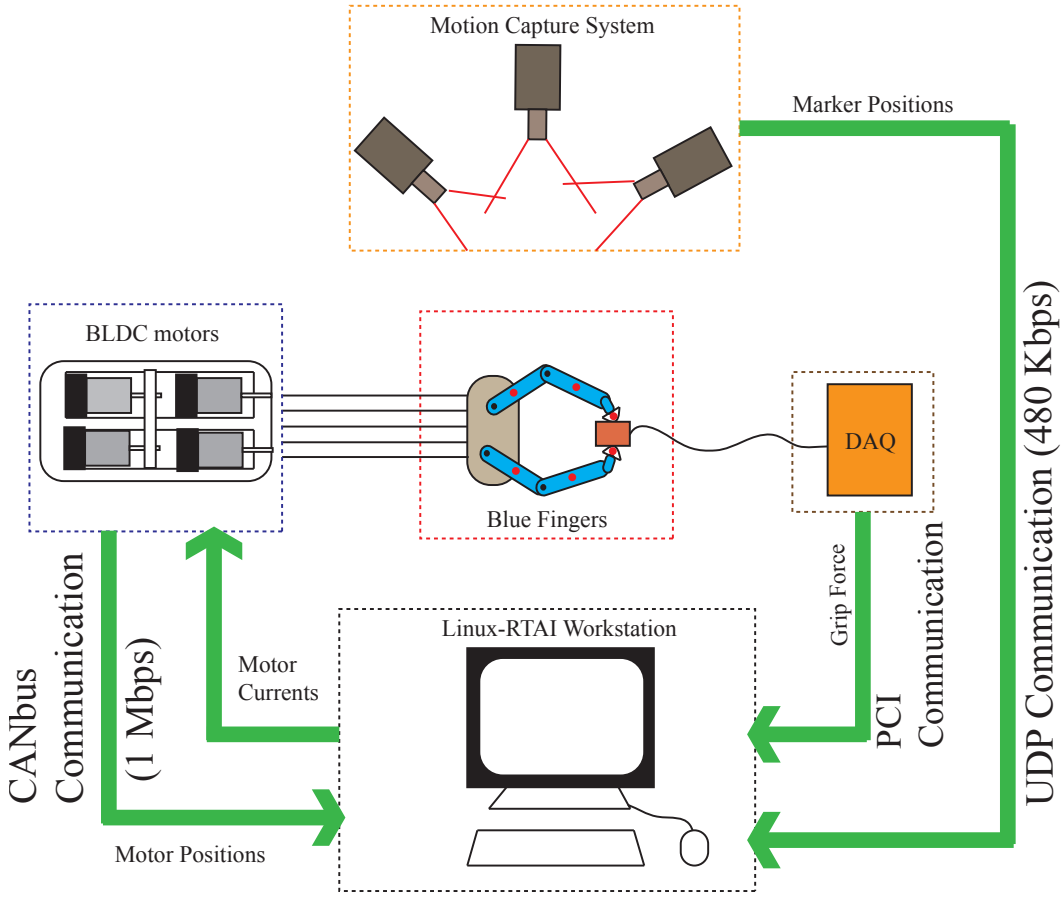

Figure 4.2: Software setup for the experiments.

4.1.1 Hardware Setup

The testbed used for conducting experiments consists of two planar, 2-DOF tendon-driven fingers with 2N tendon arrangements made using laser-cut lightweight acrylic. Elastic latex bands were used as ligaments for adding parallel compliance to the finger joints. For the 2N arrangement, a total of 8 custom-made brush-less DC motors were used. The motors were driven using the Barrett Technology Puck motor driver. The pucks were in turn controlled using the CAN bus interface at baud rates of 48 Mbps. A button load cell (Futek LLB130) fitted in a lightweight wooden block was used as the object for grasping and manipulation experiments. The load cell was then connected to a data acquisition board (National Instruments M-series PCIe-6321) to provide feedback of the applied gripping force.

One important constraint common to all robotic hands is the lack of space for proper instrumentation. Joint angle and end-tip position estimation becomes a problem in this case as joint encoders are often bulky and require complex arrangement and will increase the weight of the robotic hand. To overcome this problem, joint angle and end-tip position estimation was performed using active motion-capture system (PhaseSpace Inc.). This active motion capture system uses infrared (IR) cameras to capture IR LED markers which emit frequency-modulated light pulses encoded specifically for each LED. This enables the system to retain the correct marker identities, even when subjected to prolonged marker occlusion.

4.1.2 Grasp Stability Analysis

The contact points in this system are rolling contacts, as seen in Fig. 4.1; the fingertips are circular with some radius r_{tip}, and the object is rectangular with total width w_{obj}. To analyze the grasp stability properties of this two-fingered grasp, we use the methods proposed by Montana [15]. We assume the forces at the contact points are equal and opposite gripping forces, the contact points are diametrically opposed, and the C.O.M. is located on a line joining the two contact points.

From Montana's work, the requirements for borderline stability are as follows:

$$k_{1a}^{-1} + k_{2a}^{-1} \geq w_{obj}, \qquad k_{1b}^{-1} + k_{2b}^{-1} \geq w_{obj} \tag{4.1}$$

where the k variables are the principle relative curvatures between the fingertips and the grasped object. For this scenario, these curvatures are k_{1a} = k_{1b} = k_{2a} = k_{2b} = $1/r_{tip}$. Hence, the grasp is borderline stable if $r_{tip} \geq \frac{1}{2} w_{obj}$.

We designed our experimental testbed so that this inequality does not hold ($r_{tip} \approx$ 1.3 cm and $w_{obj} \approx$ 4.4 cm). Therefore, the active stabilization presented in the object grasping controller will need to be robust enough to overcome the borderline instability of the grasp. By addressing this more difficult control problem, we can clearly demonstrate the robustness of the active stabilization algorithm.

4.1.3 Software Setup

For accurate control programming, a real-time platform capable of performing cyclic tasks with minimum time difference between sequential loop times (jit-

ter) is required. There are a number of real-time operating systems available. For our experiments we used the Linux-RTAI (RealTime Application Interface) platform. RTAI is a Linux patch that allows for real-time programming with low jitter ($< 15\mu$s).

As the number of actuators and feedback sensors increases in systems, synchronization of data and proper communication between the computer and the hardware become paramount to the control system. Low level access to the hardware was required to be able to unify the protocols required to communicate with all the devices. We decided to utilize C/C++ to write the framework for hardware access. The motion capture marker data for finger pose estimation was accessed over the network from the remotely located server. The grip force data was accessed using the *comedi* libraries which are specialized C/C++ interface libraries for communicating with DAQs (Data Acquisition devices) in RTAI. The overall system was encapsulated in hard real-time RTAI functions for assured determinism.

The low level motor control system was designed as two modules, namely the behavior client module and the aggregation client module [5]. The behavior client module communicates with shared memory that stores the motor variables and creates virtual tendons for the user to compute and assign required forces for control. The aggregation client communicates directly with the behavior client to translate the calculated forces or positions into motor controller understandable values. Also, any changes in motor torque or position are stored in this client and then converted to meaningful tendon force values that the behavior client can use.

The low level motor control and motor parameter acquisition loop was run

at 1 KHz, while the higher level impedance control loop's frequency was decided by the maximum allowable frequency of the slowest component in the entire setup. The motion capture system allowed a maximum acquisition frequency of 480 Hz, so the higher control loop was configured to run at that frequency.

4.2 Experimental Controller Design

The previous control laws are modified to work with the experimental setup. We design a motor-level control law so that the actuators behave as close as possible to an ideal force source. Also, we moved from simple stiffness control to impedance control, allowing us to define damping terms to more fully control the system's dynamic response. A joint impedance controller is first designed for single finger motions, then an object-level impedance controller is designed for dexterous manipulation tasks.

4.2.1 Motor-Level Controller Design

For reference, the system's equations of motions were previously derived in Chapter 2, Eqs. (2.1)-(2.2) to be:

$$\mathbf{M}(\mathbf{q})\ddot{\mathbf{q}} + \mathbf{C}(\mathbf{q},\dot{\mathbf{q}}) + \boldsymbol{\tau}_k(\mathbf{q}) = \mathbf{R}\mathbf{f}_t + \mathbf{J}(\mathbf{q})^T\mathbf{f}_{ext} \tag{4.2}$$

$$\mathbf{J}_m\ddot{\boldsymbol{\theta}} + \boldsymbol{\tau}_{\theta,fr} + \mathbf{P}_m\mathbf{f}_t = \boldsymbol{\tau}_{\theta,m} \tag{4.3}$$

Given a desired joint torque $\boldsymbol{\tau}_{q,des}$ to be applied by the tendons, the desired motor torques can be defined as

$$\boldsymbol{\tau}_{\theta,m} = \mathbf{P}_m(\mathbf{R}^+\boldsymbol{\tau}_{q,des} + \mathbf{f}_{int}) + \hat{\boldsymbol{\tau}}_{\theta,fr} + \mathbf{J}_m\ddot{\boldsymbol{\theta}}_m \tag{4.4}$$

where $\hat{\boldsymbol{\tau}}_{\theta,fr}$ is an experimentally-determined motor friction compensation term. In practice, the frictional torque dominates the motor inertia term $\mathbf{J}_m\ddot{\boldsymbol{\theta}}_m$, so inertia is neglected.

With the 2N tendon arrangement, the internal forces $\mathbf{f}_{int}$ are found by applying equivalent pulling forces to antagonistic tendon pairs. In order to limit the tendon tensions to some range $0 \leq f_{min} \leq f_t \leq f_{max}$, a joint torque scaling method is used, as presented in [1]. Joint torque scaling preserves the direction of endpoint forces produced by the actuators at the fingertip, which would not be the case if the individual motors were simply saturated at their torque limits.

Given some desired torques $\boldsymbol{\tau}_{q,des}$, the optimization function to determine the scaling factor α is given by:

$$\begin{aligned} &\text{maximize} \quad \alpha \in (0,1] \\ &\text{subject to} \quad \boldsymbol{\tau}_{scaled} = \alpha\boldsymbol{\tau}_{q,des} = \mathbf{R}\mathbf{f}_t \\ &\qquad\qquad f_{t,i} \in [f_{min}, f_{max}] \text{ for } i = 1, ..., n \end{aligned} \tag{4.5}$$

4.2.2 Single Finger Joint Impedance Controller Design

Next, a higher-level control law is designed to generate $\boldsymbol{\tau}_{q,des}$ to be used by the previous motor-level control. An active joint impedance control law can be specified as

$$\boldsymbol{\tau}_{q,des} = \mathbf{K}_d\tilde{\mathbf{q}} + \mathbf{B}_d\dot{\tilde{\mathbf{q}}} + \mathbf{M}\ddot{\mathbf{q}}_d + \mathbf{C}(\mathbf{q},\dot{\mathbf{q}}) + \hat{\boldsymbol{\tau}}_k(\mathbf{q}) \tag{4.6}$$

where $\hat{\boldsymbol{\tau}}_k(\mathbf{q})$ is the estimated joint stiffness term and $\tilde{\mathbf{q}} = \mathbf{q}_{des} - \mathbf{q}$.

Substituting this into Eq. (4.2), while assuming a perfect joint stiffness

model ($\hat{\boldsymbol{\tau}}_k = \boldsymbol{\tau}_k$) and assuming an effective motor-level controller such that $\boldsymbol{\tau}_{q,des} = \mathbf{R}\mathbf{f}_t$, we find the closed-loop system equation as follows:

$$\mathbf{M}(\mathbf{q})\ddot{\tilde{\mathbf{q}}} + \mathbf{B}_d\dot{\tilde{\mathbf{q}}} + \mathbf{K}_d\tilde{\mathbf{q}} = 0 \tag{4.7}$$

This represents stable error dynamics in the form of a user-defined impedance behavior at the joint level for chosen positive definite matrices $\mathbf{K}_d$ and $\mathbf{B}_d$. Note that in practice, the inertial terms $\mathbf{M}\ddot{\mathbf{q}}_d$ and $\mathbf{C}(\mathbf{q},\dot{\mathbf{q}})$ can be neglected from the control law in Eq. (4.6), as the low finger inertia makes these terms an order of magnitude smaller than other terms.

In the next section, we expand this controller to a more complex two-fingered system grasping and manipulating an object.

4.2.3 Object-Level Impedance Controller Design

We modified the object-level stiffness controller in Section 3.2.1 to an object impedance control law of the following form:

$$\mathbf{f}_{imp} = \mathbf{W}^{+}(\mathbf{K}_d(\mathbf{z}_{des} - \mathbf{z}) + \mathbf{B}_d(\dot{\mathbf{z}}_{des} - \dot{\mathbf{z}})) \tag{4.8}$$

where matrices $\mathbf{K}_d = diag(K_x, K_y, K_\phi)$ and $\mathbf{B}_d = diag(B_x, B_y, B_\phi)$ contain the object stiffness and damping gains, respectively. Then, as before in Eq. (3.8), the four desired joint torques are:

$$\boldsymbol{\tau}_{q,des} = \mathbf{J}^T\Big(\mathbf{f}_{imp} + \begin{bmatrix}\mathbf{f}_{grip,1}\\ \mathbf{f}_{grip,2}\end{bmatrix}\Big) + \begin{bmatrix}\tau_{k,1}(\mathbf{q_1})\\ \tau_{k,2}(\mathbf{q_2})\end{bmatrix} \tag{4.9}$$

In a real system, force feedback is necessary to maintain accurate grip forces in the presence of disturbances or model errors. Assuming the applied grip force

is being measured using a force sensor as f_s, we can define f_{int} as a proportional-integral (PI) force feedback:

$$f_{int} = f_{des} + K_{f,p}(f_{des} - f_s) + K_{f,i} \int (f_{des} - f_s) \tag{4.10}$$

This gripping force f_{int} needs to be produced at each fingertip such that their combined effect produces no net force or moment on the grasped object. To achieve this, we specify $\lambda_i = 0$ and $f_i = f_{int}$ for each finger and use Eq. (2.5):

$$\mathbf{f}_{ci} = \begin{bmatrix} \cos(\phi) & -\sin(\phi) \\ \sin(\phi) & \cos(\phi) \end{bmatrix} \begin{bmatrix} (-1)^{i+1} f_i \\ \lambda_i \end{bmatrix}$$

This returns two internal force vectors $\mathbf{f}_{grip,i}$ (i=1,2) to be applied by the controller, acting in equal and opposite directions on a line of action passing through the contact points.

Object position and orientation information is being sensed using the motion capture system, which has an inherent time lag and fixed sampling rate. If we try to differentiate the motion capture data to obtain velocity values for the damping terms, this time lag can result in stability issues. Therefore, we instead use the motor velocities using filtered position data from motor encoders, and then transform them to the fingertip (x,y) frame.

$$\begin{bmatrix} v_{x,tip,i} \\ v_{y,tip,i} \end{bmatrix} = \mathbf{J}_i(\mathbf{q}_i)\mathbf{R}^{T+}\mathbf{P}_m\dot{\boldsymbol{\theta}}_m \tag{4.11}$$

Note that this transformation is only valid with non-compliant tendons, as tendon stretching is not accounted for.

To further reduce the damping terms' reliance upon the motion capture data, we apply the damping terms to the fingertip velocities instead of to object coordinates. Letting $\mathbf{v}_{tip} \in \mathbb{R}^4$ be the vector of actual fingertip velocities calculated in Eq.

(4.11), and knowing the desired fingertip velocities can be found from the desired object trajectory as $\mathbf{v}_{tip,des} = \mathbf{W}^T\dot{\mathbf{z}}_{des}$, Eq. (4.8) changes to

$$\mathbf{f}_{imp} = \mathbf{W}^{+}\mathbf{K}_d(\mathbf{z}_{des} - \mathbf{z}) + \mathbf{B}_{d,tip}(\mathbf{W}^T\dot{\mathbf{z}}_{des} - \mathbf{v}_{tip}) \tag{4.12}$$

Additionally, a lag in the motion capture data of $\approx$ 15 ms causes issues with the already naturally unstable object orientation stabilization. In practice, by combining an integral term with the proportional $K_\phi(\phi_{des} - \phi)$ term, the grasp can be maintained more robustly even in the presence of time lag and a limited sampling rate. Finally, the calculated desired joint torques $\boldsymbol{\tau}_{q,des}$ found using Eqs. (4.9)-(4.12) are sent to the motor-level control law in Eq. (4.4) to determine the commanded actuator inputs.

4.3 Experimental Results

This section presents the results of our experimental testbed. We first ran tests to determine motor friction and joint stiffness parameters for effective compensation in the control algorithm. Then, single finger joint tracking tasks were performed to verify our impedance control law, along with object manipulation tasks for trajectory tracking and disturbance rejection. In each case, we performed experiments both with and without parallel joint compliance in order to isolate the effect of parallel compliance on finger performance and robustness.

4.3.1 Motor Friction Compensation

While the custom brushless DC motors used in these experiments are capable of generating the high torques required for stable grasping while retaining backdriveability, they also introduce nonlinear effects such as friction and motor cogging. Motor stiction in particular makes force control inaccurate, and without compensation would require high controller gains to overcome.

Conventionally, the frictional torque of each motor is defined as a combination of static friction and Coulomb friction. In addition, the tendon forces f_t apply a transverse load to the motor axles, increasing bearing friction. Assuming this effect is linear,

$$\tau_{\theta,fr} = r_m(a + b \cdot f_t) \cdot \text{sign}(\dot{\theta}_m) + \tau_c(\dot{\theta}_m, f_t) \tag{4.13}$$

where a and b are experimentally determined friction constants and τ_c is a function representing Coulomb friction.

We modified this classical friction equation for physical implementation in our system. The primary function of our friction compensation is to overcome stiction. Therefore, the more linear Coulomb friction components, τ_c, are not compensated for because they act as damping elements and will only increase the system's stability. In addition, this friction model is dependent on the sign of each motor's velocity. Because we would like to overcome stiction, we need a friction compensation torque that will be active even when the motor is not moving ($\dot{\theta}_m$ = 0). To accomplish this, the $\dot{\theta}_m$ term is replaced with ($\theta_{m,des} - \theta_m$); in this way, the friction compensation term will act in the direction of the motor position error. Finally,

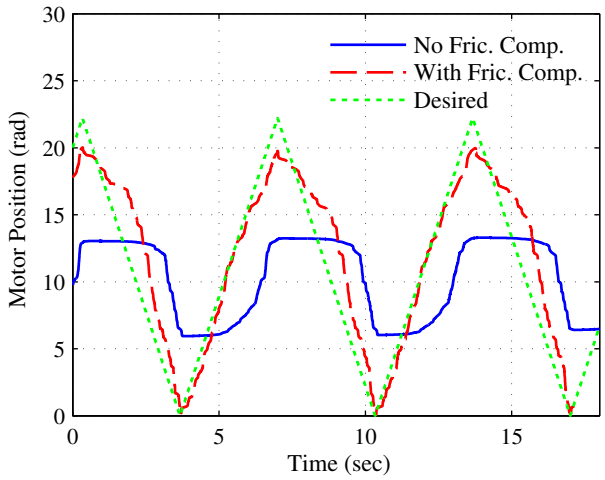

Figure 4.3: Friction compensation testing for a single motor, with a grounded linear spring acting as the load torque and a triangular commanded motor torque profile. The friction constants for Eq. (4.13) were found experimentally as $(a, b) \approx (0.94\ N, 0.0033)$.

to smooth the effects of switching conditions, we replace the *sign* function with a *tanh* function with a tuneable δ parameter. Combining these changes, the friction compensation torque used by the controller for each motor is

$$\hat{\tau}_{\theta,fr} = r_m(a + b \cdot f_t) \cdot \tanh(\frac{\theta_{m,des} - \theta_m}{\delta}) \tag{4.14}$$

In the absence of tendon tension sensing, an accurate friction model is critical to ensure the commanded tendon tensions are in fact being transmitted to the fingers. This is illustrated by the friction compensation test for a single motor shown in Figure 4.3.

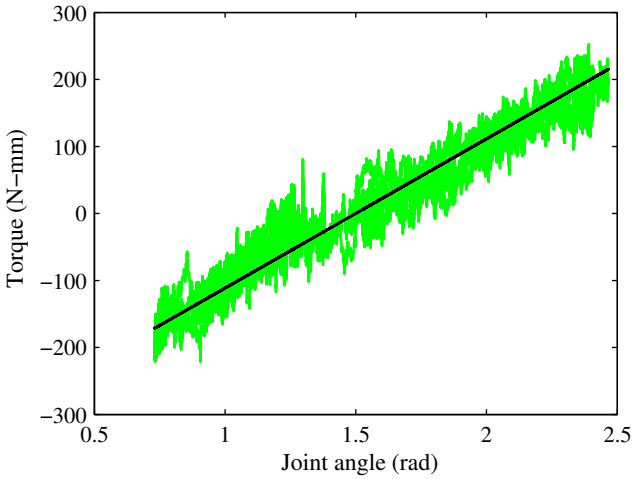

Figure 4.4: Compliance identification data for joint q_{21}, along with a linear data fit that will be used in the control law.

4.3.2 Joint Compliance Identification

From Eq. (4.6), the control law needs an estimated joint stiffness $\hat{\boldsymbol{\tau}}_k(\mathbf{q})$ to properly account for the passive parallel compliance and limit steady-state tracking errors. To find the stiffness model of the elastic ligaments (see Fig. 4.1(C)), experiments were performed with a force sensor to find the relationship between applied torque and joint angle. An example is shown in Fig. 4.4. A linear regression was used to fit the data and provide an estimated stiffness model to be used by the controller.

4.3.3 Experimental Results

The following experiments are designed to isolate the effects of parallel joint compliance, with trajectory tracking and robustness to impact as the performance metric. The control laws in Sections 4.2.2 and 4.2.3 are designed to produce the

same effective impedance behavior with or without the presence of joint compliance. Therefore, because the theoretical closed-loop behavior of the system should be identical with or without passive compliance, we are able to isolate the effects of parallel joint compliance in the system with all other conditions being equal.

4.3.3.1 Single Finger Trajectory Tracking

First, single finger joint trajectory tracking experiments were performed as shown in Fig. 4.5, comparing the cases with and without the presence of parallel joint compliance. The commanded sinusoidal paths for the two joints are at different frequencies, such that the finger moves through a more complete range of motion. Although we may expect that adding an imperfectly modeled compliant element would degrade the tracking performance, the two trajectories are nearly identical.

4.3.3.2 Object Manipulation Trajectory Tracking

To identify the effects of parallel compliance during environmental interaction, a more difficult object grasping and manipulation experiment was performed. Two-fingered grasping experiments in Fig. 4.6 compare the trajectory tracking with and without the presence of joint compliance parallel to the actuators. The desired object trajectory in this case is a circular path, coupled with changes in the object's orientation. The frequency of the commanded circular path and object orientation are at different frequencies to produce a different motion every cycle.

The tracking errors are similar in each case, showing that even using a lin-

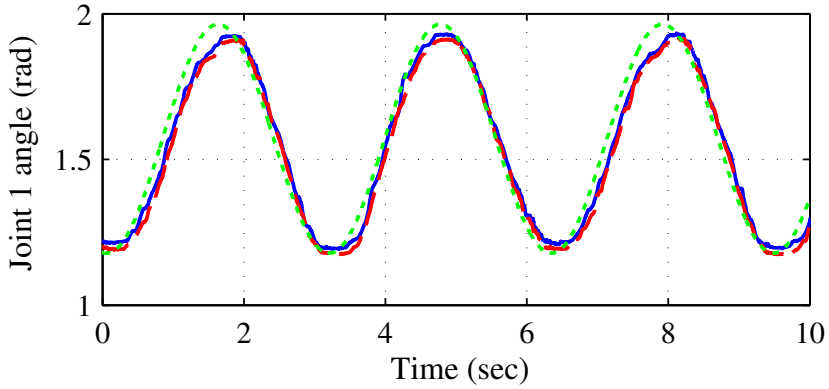

(a)

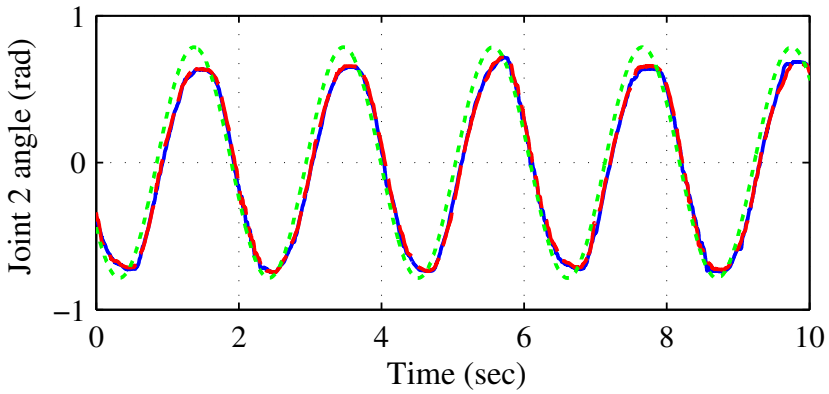

(b)

Figure 4.5: Single finger trajectory tracking comparison without joint compliance (solid blue line) and with joint compliance (red dashed line).

ear approximation of joint compliance, performance can be maintained. The differences are seen in the smoothness of the motions in the case with parallel compliance. Focusing on the enlarged plots in Fig. 4.7, we can see that the object orientation shows oscillations without compliance which do not occur with parallel compliance.

The position spikes seen in the non-compliant case could arise from various sources, such as unmodeled dynamics, errors in friction compensation, limited sampling rate, and control loop latencies. By using mechanical compliance, which has an instantaneous reaction time, these disturbances can be handled more robustly by the combined efforts of the control system and mechanical compliance. These results are repeatable for any commanded motions. The parallel joint compliance consistently resulted in more stable grasping and smoother finger motions.

4.3.3.3 Object Grasping Impact Testing

To analyze the fingers' robustness to impacts, the system was given approximately identical impacts while attempting to maintain constant grasp force and object position/orientation. Figure 4.8 shows an example impact response. The compliant case shows significant improvements in settling time of the system, especially with regard to the naturally unstable object orientation. Figure 4.9 shows a response when subjected to a larger impact. This larger impact causes instability and loss of contact in the non-compliant fingers, while the fingers with parallel compliance robustly maintain the desired grasp and return to the desired object position.

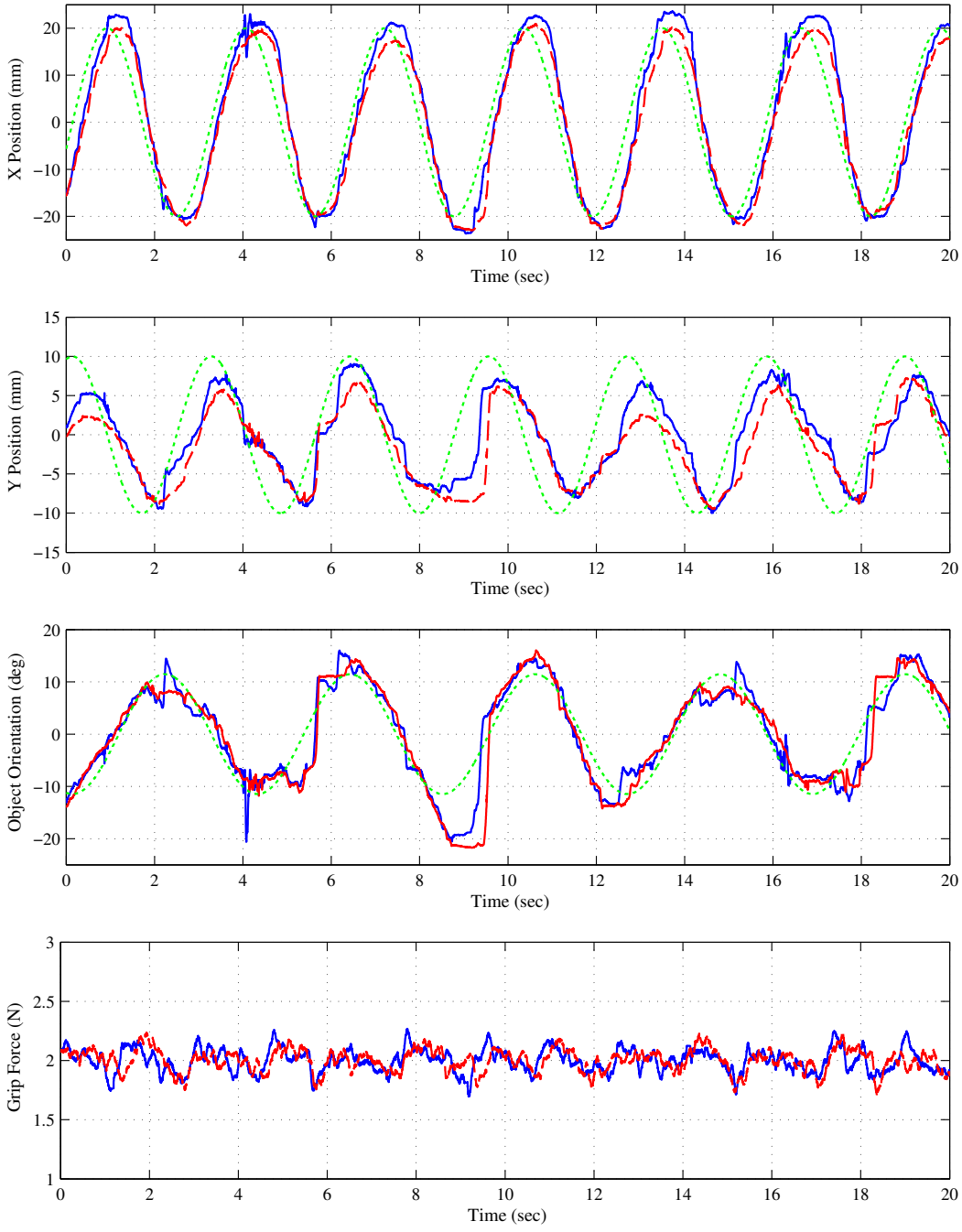

Figure 4.6: Object grasping trajectory tracking comparison without joint compliance (solid blue line) and with joint compliance (red dashed line).

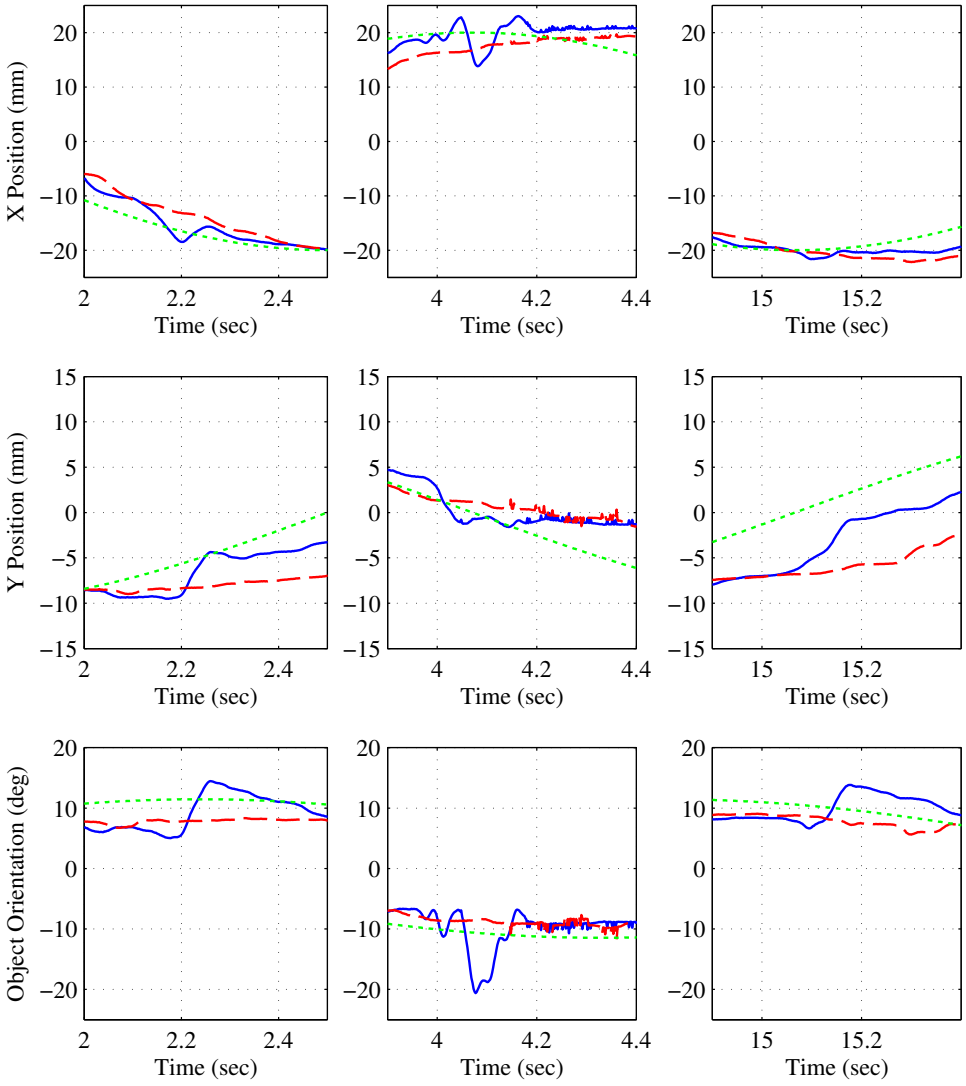

Figure 4.7: Enlarged views at critical points of the object grasping trajectory tracking comparison without joint compliance (solid blue line) and with joint compliance (red dashed line). These time intervals show the lower stability of the finger-object system without joint compliance, especially considering object orientation.

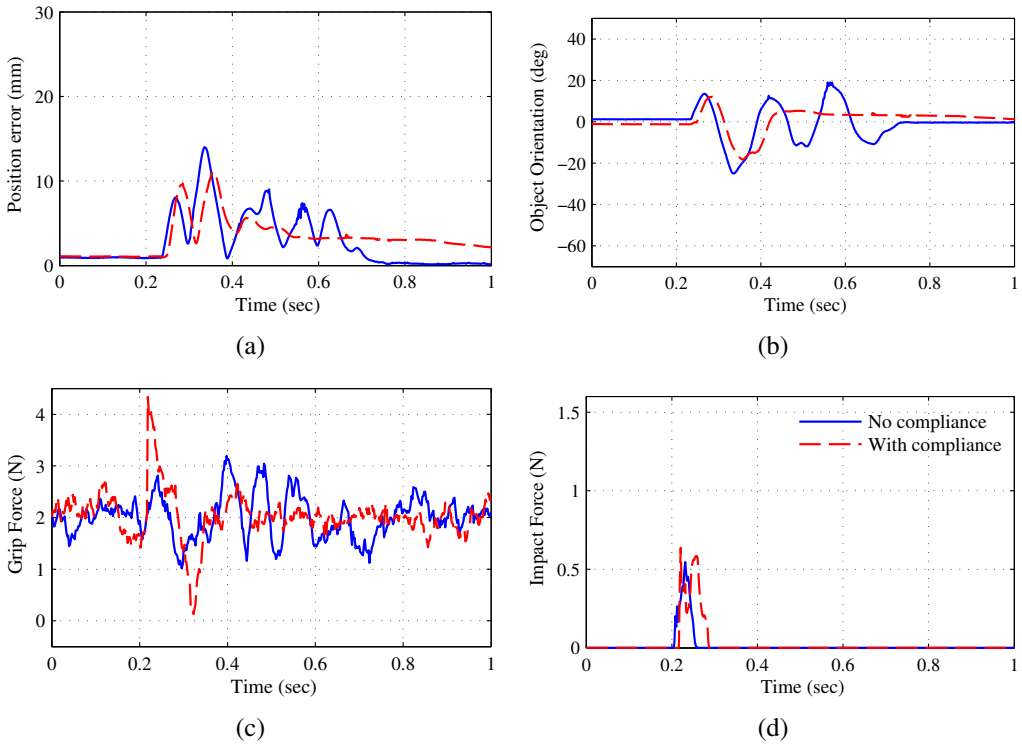

Figure 4.8: Object grasping disturbance response with and without joint compliance, given approximately equivalent impacts.

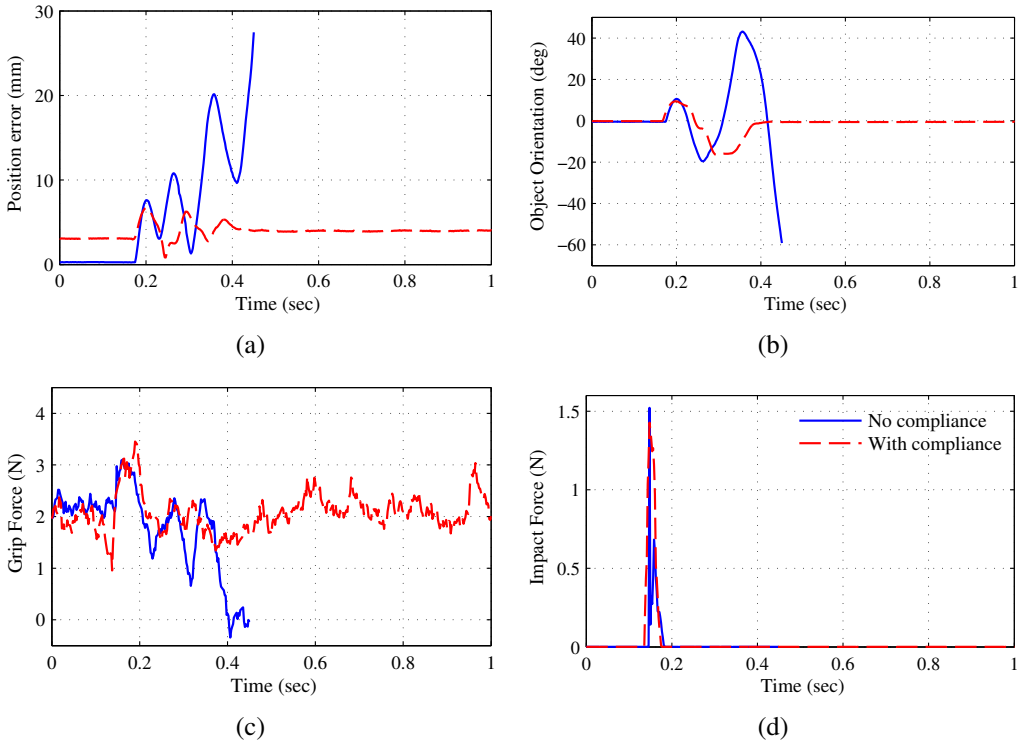

Figure 4.9: Object grasping impulse disturbance response with and without joint compliance, given a larger impact force. The no compliant case showed instability and loss of contact.

Chapter 5

Conclusions

Through simulation studies and experimentation, we have demonstrated that the integration of passive parallel compliance leads to improved stability and disturbance rejection in robotic fingers. For a 2-DOF finger, a simulation analysis was performed to compare cases with active stiffness control laws with varying controller frequencies. Active stiffness control is designed to emulate passive mechanical springs, but a passivity analysis showed that with a limited controller frequency, the actuators add net energy to the system and can cause system instability. We extended this to a more complex two-fingered pinching grasp using object-level stiffness control. Simulation results show that fingers with mechanical compliance arranged in parallel to the actuators show improved stability when subjected to external disturbances.

To validate these findings experimentally, we built an experimental testbed consisting of two 2-DOF tendon-driven robotic fingers. A unified software framework was developed for deterministic control while accessing and sending data to and from multiple sources (motion capture system, DAQ, and motor controller). We then mathematically modeled the system consisting of the two fingers with parallel joint compliance present and grasping an object. This model was used to develop an

impedance controller for use in grasping and manipulation experiments. By choosing an object larger than the minimum bound for borderline grasp stability, we addressed a challenging control problem and clearly demonstrated the robustness of our controller. To improve the accuracy of actuator forces, we designed a novel friction compensation technique that overcomes bearing friction caused by transverse tendon forces and utilizes motor position rather than velocity to overcome stiction.

This is the first time experiments have been carried out to analyze the effects of parallel joint compliance in robotic fingers performing dexterous manipulation tasks. The experimental results confirm that parallel joint compliance improves the stability, produces smoother trajectory tracking, and improves robustness to disturbances for robotic fingers during a two-fingered grasping task. This is an important step toward reaching the goal of human-like hand dexterity with robotic hands.

These results are also applicable to robotic fingers with a variety of actuation and transmission arrangements. Robotic fingers with backdriveable actuators and low tendon compliance may benefit by implementing parallel compliance. Hands with compliant tendons (series compliance) and nonbackdriveable actuators would also benefit from the increased stability provided by implementing parallel compliance, especially when interacting with the environment during manipulation tasks.

Bibliography

[1] M.E. Abdallah, R. Platt, C.W. Wampler, and B. Hargrave. Applied joint-space torque and stiffness control of tendon-driven fingers. In *IEEE-RAS International Conference on Humanoid Robots (Humanoids)*, pages 74–79, 2010.

[2] A. Albu-Schaffer, O. Eiberger, M. Grebenstein, S. Haddadin, C. Ott, T. Wimbock, S. Wolf, and G. Hirzinger. Soft robotics. *IEEE Robotics Automation Magazine*, 15(3):20–30, 2008.

[3] S. Arimoto, K. Tahara, J.-H. Bae, and M. Yoshida. A stability theory of a manifold: concurrent realization of grasp and orientation control of an object by a pair of robot fingers. *Robotica*, 21(02):163–178, 2003.

[4] A. Bicchi and V. Kumar. Robotic grasping and contact: a review. In *IEEE International Conference on Robotics and Automation (ICRA)*, volume 1, pages 348–353, 2000.

[5] T. Blakely and Y. Matsuoka. Software framework for human neuromuscular behavior. In *IEEE International Conference on Robotics and Automation (ICRA)*, pages 4069–4073, 2009.

[6] M. Chalon, W. Friedl, J. Reinecke, T. Wimboeck, and A. Albu-Schaeffer. Impedance control of a non-linearly coupled tendon driven thumb. In

IEEE/RSJ International Conference on Intelligent Robots and Systems (IROS), pages 4215–4221, 2011.

[7] M.R. Cutkosky and Imin Kao. Computing and controlling compliance of a robotic hand. *IEEE Transactions on Robotics and Automation*, 5(2):151–165, 1989.

[8] Aaron M. Dollar and Robert D. Howe. The highly adaptive SDM hand: Design and performance evaluation. *The International Journal of Robotics Research*, 29(5):585–597, April 2010.

[9] M. Grebenstein, A. Albu-Schaffer, Thomas Bahls, M. Chalon, O. Eiberger, W. Friedl, R. Gruber, S. Haddadin, U. Hagn, R. Haslinger, H. Hoppner, S. Jorg, Mathias Nickl, Alexander Nothhelfer, F. Petit, J. Reill, N. Seitz, T. Wimbock, S. Wolf, T. Wusthoff, and G. Hirzinger. The DLR hand arm system. In *IEEE International Conference on Robotics and Automation (ICRA)*, pages 3175–3182, 2011.

[10] Neville Hogan. Impedance control: An approach to manipulation. *Journal of Dynamic Systems, Measurement, and Control*, 107:1–24, 1985.

[11] R. S. Johansson and G. Westling. Programmed and triggered actions to rapid load changes during precision grip. *Experimental Brain Research*, 71(1):72–86, June 1988.

[12] E. R. Kandel, J. H. Schwartz, and T. M. Jessell. *Principles of Neural Engineering*. McGraw Hill, New York, fourth edition, 2000.

[13] Pei-Hsin Kuo and A.D. Deshpande. Contribution of passive properties of muscle-tendon units to the metacarpophalangeal joint torque of the index finger. In *3rd IEEE/RAS and EMBS International Conference on Biomedical Robotics and Biomechatronics (BioRob)*, pages 288–294, 2010.

[14] Fabrizio Lotti, Paolo Tiezzi, Gabriele Vassura, Luigi Biagiotti, Gianluca Palli, and Claudio Melchiorri. Development of UB hand 3: Early results. In *IEEE International Conference on Robotics and Automation (ICRA)*, page 44884493, 2005.

[15] D.J. Montana. Contact stability for two-fingered grasps. *IEEE Transactions on Robotics and Automation*, 8(4):421–430, 1992.

[16] JungJun Park, ByeongSang Kim, JaeBok Song, and HongSeok Kim. Safe link mechanism based on passive compliance for safe human-robot collision. In *IEEE International Conference on Robotics and Automation (ICRA)*, 2007.

[17] G.A. Pratt and M.M. Williamson. Series elastic actuators. In *IEEE/RSJ International Conference on Intelligent Robots and Systems (IROS). 'Human Robot Interaction and Cooperative Robots'*, volume 1, pages 399–406 vol.1, 1995.

[18] Stanley A. Schneider and Robert H. Cannon Jr. Object impedance control for cooperative manipulation: Theory and experimental results. *IEEE Transactions on Robotics and Automation*, 8(3):383–394, 1992.

[19] Luis Sentis, Jaeheung Park, and Oussama Khatib. Compliant control of multi-

contact and center-of-mass behaviors in humanoid robots. *IEEE Transactions on Robotics*, 26(3):483–501, June 2010.

[20] K. Tahara, Zhi-Wei Luo, R. Ozawa, Ji-Hun Bae, and S. Arimoto. Bio-mimetic study on pinching motions of a dual-finger model with synergistic actuation of antagonist muscles. In *IEEE International Conference on Robotics and Automation (ICRA)*, pages 994–999, 2006.

[21] D. Williams and O. Khatib. The virtual linkage: a model for internal forces in multi-grasp manipulation. In *IEEE International Conference on Robotics and Automation (ICRA)*, pages 1025–1030 vol.1, 1993.

[22] Thomas Wimboeck, Christian Ott, and Gerd Hirzinger. Passivity-based object-level impedance control for a multifingered hand. In *IEEE/RSJ International Conference on Intelligent Robots and Systems (IROS)*, page 46214627, 2006.

[23] Ikuo Yamano and Takashi Maeno. Five-fingered robot hand using ultrasonic motors and elastic elements. In *IEEE International Conference on Robotics and Automation (ICRA)*, page 26732678, 2005.

Vita

Taylor Douglas Niehues was born in San Angelo, Texas. After graduating from Glasscock County I.S.D., Garden City, TX, in 2007, he entered Texas Tech University in Lubbock, Texas. He received the degree of Bachelor of Science in Mechanical Engineering from Texas Tech University in 2011. In August, 2011, was accepted into the Mechanical Engineering Graduate Program at The University of Texas at Austin.

Email: taylor.niehues@utexas.edu

This thesis was typeset by the author.